Design of Cu2O–Au Composite Microstructures for Surface-Enhanced Raman Scattering Study

Article *in* Colloids and Surfaces A Physicochemical and Engineering Aspects · July 2016

DOI: 10.1016/j.colsurfa.2016.07.053

CITATION
1

READS
34

10 authors, including:

Lei Chen
Jilin Normal University
57 PUBLICATIONS **483** CITATIONS
SEE PROFILE

Yongjun Zhang
112 PUBLICATIONS **1,300** CITATIONS
SEE PROFILE

Yang Liu
Wayne State University
454 PUBLICATIONS **3,527** CITATIONS
SEE PROFILE

Xiaoyan Liu
Jilin Normal University
43 PUBLICATIONS **619** CITATIONS
SEE PROFILE

Colloids and Surfaces A: Physicochem. Eng. Aspects 507 (2016) 96–102

Contents lists available at ScienceDirect

Colloids and Surfaces A: Physicochemical and Engineering Aspects

journal homepage: www.elsevier.com/locate/colsurfa

Design of Cu_2O-Au composite microstructures for surface-enhanced Raman scattering study

Lei Chen [a], Yue Zhao [a], Yongjun Zhang [a,*], Maomao Liu [a], Yaxin Wang [a], Xin Qu [b,c], Yang Liu [a], Ji Li [a], Xiaoyan Liu [a], Jinghai Yang [a,b]

[a] Key Laboratory of Functional Materials Physics and Chemistry, Jilin Normal University, Ministry of Education, Siping 136000, PR China
[b] Changchun Institute of Optics, Fine Mechanics and Physics, Chinese Academy of Sciences, Changchun 130033, PR China
[c] University of Chinese Academy of Sciences, Beijing 100039, PR China

HIGHLIGHTS

- Octahedral Cu_2O-Au composite microstructures were synthesized with a facile *in situ* method.
- Charge transfer from Au to Cu_2O.
- A combination of electromagnetic and chemical enhancement mechanisms occurred at the interface.

GRAPHICAL ABSTRACT

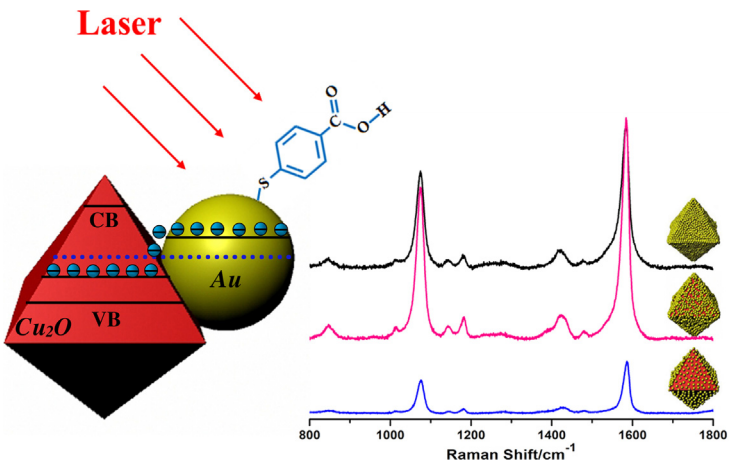

ARTICLE INFO

Article history:
Received 25 April 2016
Received in revised form 14 July 2016
Accepted 19 July 2016
Available online 20 July 2016

Keywords:
Cu_2O-Au composite microstructures
Surface-enhanced raman scattering
Localized surface plasmon resonance
Charge transfer

ABSTRACT

Octahedral Cu_2O-Au composite microstructures (CMSs) were synthesized with a facile *in situ* method and were attempted as surface-enhanced Raman scattering (SERS) substrates. The density of the Au nanoparticles (NPs) on the surface of the octahedral Cu_2O microcrystals can be controlled by tuning the concentration of the gold precursor, which can further influence the SERS activity of the Cu_2O-Au CMSs system. The CMSs system exhibited a charge transfer from Au to Cu_2O. Furthermore, metallic NPs deposited on the semiconductor material formed a local electromagnetic field, which altered the interfacial charge distribution. The SERS signal enhancement from the Cu_2O-Au CMSs system is attributed to a combination of electromagnetic and chemical enhancement mechanisms occurring simultaneously at the semiconductor-metal interface. Overall, the proposed CMSs system will provide a new model for SERS study and application.

1. Introduction

Surface-enhanced Raman scattering (SERS) has been proven to be a versatile and powerful tool for serving frontier science such

* Corresponding author.
E-mail address: yjzhang@jlnu.edu.cn (Y. Zhang).

http://dx.doi.org/10.1016/j.colsurfa.2016.07.053
0927-7757/

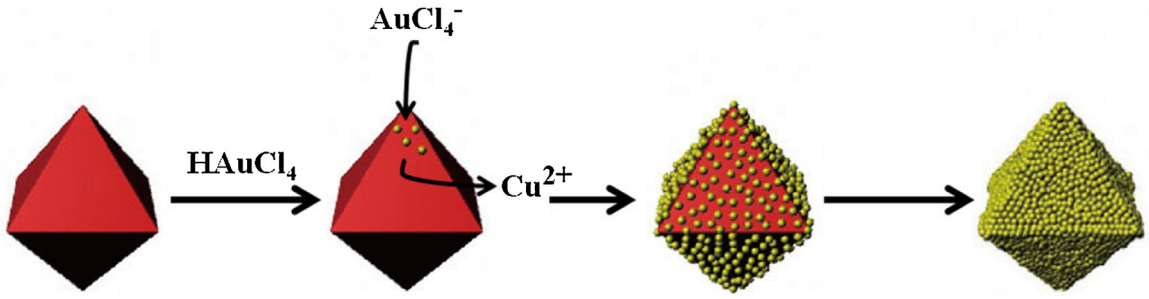

Scheme 1. Schematic illustration of the growth process of the Au NPs on the octahedral Cu_2O microcrystals.

as surface science, analytical chemistry, electrochemistry, and biological systems [1–6]. SERS has recently received much attention because of its considerable potential in the highly sensitive and selective detection of molecules, including single-molecule detection [3,4]. The enhancement of the Raman signal from a SERS-active substrate is generally attributed to two different factors: electromagnetic (EM) and chemical enhancements [7–9], which involve the localized surface plasmon resonance (LSPR) and the charge-transfer (CT) effect, respectively.

Generally, the capabilities of SERS depend on the performance characteristics of the SERS-active substrate. Metal nanoparticles (NPs, gold, silver, or copper) with distinctive LSPR were widely used as SERS substrates due to their extremely strong enhancement [10–12]. LSPR, which was used to measure the collective electron charge oscillations in metallic NPs excited by laser, has been important in the analytical application of SERS. LSPR depends primarily on the size, shape, composition, and medium of the NPs. Though the semiconductor materials have also been studied and applied as SERS substrates, their SERS enhancement is much lower than the metal NPs [13–15]. However, multicomponent nanostructures can incorporate multiple functions into one system for specific applications and fascinating new properties induced by heterointerfaces [16–20]. Therefore, to improve the SERS activity of semiconductors and optimize the LSPR property of the metal NPs, semiconductor-metal composites are synthesized to study their improved SERS enhancements. After the metal NPs are deposited on the surface of the semiconductor, charge transfer occurs until the two systems are equilibrated, which induces a higher charge density region located adjacent to the junction, and therefore the semiconductor-metal composites will exhibit enhanced SERS due to their special structures [16,18,19].

In addition, semiconductor-metal composites exhibited different SERS enhancements for the CT effect. Recently, most semiconductor-metal compositions were introduced as SERS-active substrates. In the Ag/CuO nanocomposite system [16], electrons transferred from Ag to CuO until the two systems achieved equilibration. This charge redistribution resulted in the junction of a positively charged Ag and a negatively charged CuO, where the highest charge density excited a more intense LSPR. An extraordinary SERS enhancement phenomenon was also observed in the urchin-like Ag NPs/ZnO hollow nanosphere arrays [18]. When the Ag NPs came into contact with ZnO, the charge transferred from Ag to ZnO until the two systems attained equilibration. In this manner, under the irradiation with visible light, the local electromagnetic field at the interface between Ag and ZnO can be strongly improved by the charge transfer-induced polarization, thus undoubtedly enhancing the SERS intensity. Furthermore, the enhancement of the Raman signals of ZnO/Ag nanocomposites was studied [19]. Compared to pure ZnO, the ZnO/Ag nanocomposites showed SERS due to the formation of a local electric field at the interface between ZnO and Ag.

Cu_2O is broadly applied in many fields such as catalysts, sensors, and solar energy conversion [20–25]. However, few studies using Cu_2O as SERS substrates were reported, due to its weak SERS activity [26,27]. To improve the SERS activity of Cu_2O, metal NPs are employed to synthesize Cu_2O-metal heterostructures [28,29].

Herein, Au NPs were chosen to deposit on the surface of the octahedral Cu_2O microcrystals to form Cu_2O-Au composite microstructures (CMSs) for the SERS study. Cu_2O can reduce $AuCl_4^-$ at the room temperature. The Au NP products were coated on the surface of the octahedral Cu_2O microcrystals to reduce the surface energy in the system. By tuning the added volume of the gold precursor, the density of the Au NPs can be controlled, which can further tune the SERS activity of the Cu_2O-Au CMSs system. The SERS properties of 4-MBA adsorbed on the Cu_2O-Au CMSs were investigated. When the additional volume of gold precursor reached 3.00 mL, the synthesized CMSs exhibited the highest SERS property.

2. Experiment

2.1. Materials

Copper sulfate pentahydrate ($CuSO_4{\cdot}5H_2O$), polyvinylpyrrolidone (PVP, K30), sodium citrate ($Na_3C_6H_5O_7{\cdot}2H_2O$), sodium carbonate ($Na_2CO_3$), and absolute ethanol (C_2H_6O) were purchased from Sinopham Chemical Reagent Co., Ltd. Chloroauric acid ($HAuCl_4{\cdot}4H_2O$, 99.9%) was purchased from Shanghai Civi Chemical Technology Co., Ltd. Glucose ($C_6H_{12}O_6{\cdot}H_2O$) was purchased from Beijing Chemical Reagent Co., Ltd. 4-Mercaptobenzoic acid (4-MBA) was purchased from Sigma-Aldrich Chemical Co., Ltd. All the chemicals were used as received and without further purification. Deionized water was used throughout the present study.

2.2. Synthesis of octahedral Cu_2O microcrystals and Cu_2O-Au CMSs

2.2.1. Octahedral Cu_2O microcrystals

Octahedral Cu_2O microcrystals were synthesized according to the previous report by Sui [30]. That is, 0.68 g of copper sulfate pentahydrate was dispersed in 76 mL of deionized water. Then, 4.0 mL of a solution of 0.74 M sodium citrate and 1.2 M sodium carbonate was added dropwise into the mixture. A dark blue solution soon appeared, whereas no precipitate was observed. After the mixture was stirred for 10 min, 6.0 g of PVP was introduced. After the complete dissolution of the powder of PVP, 4.0 mL of 1.4 M glucose solution was slowly injected into the mixture. Thereafter, the mixture was kept in a water bath at a temperature of 80 °C for 15 min, then cooled down to the room temperature. The brick red precipitate (Fig. S1a, Supplementary information (SI)) was filtered off, then washed with deionized water and absolute ethanol, and finally dried in a vacuum at 60 °C for 6 h.

2.2.2. Cu_2O-Au CMSs

In the case of the synthesis of Cu_2O-Au CMSs, the dried octahedral Cu_2O microcrystals were firstly dissolved in 100 mL of the deionized water. Thereafter, 1% $HAuCl_4{\cdot}4H_2O$ solution was added dropwise into the mixture under vigorous stirring. The mixture was stirred at the room temperature for 2 min. There was an immediate color change from brick red to black (Fig. S1, SI), suggesting that the formation of uniform Cu_2O-Au CMSs. The products were filtered off, then washed with deionized water and absolute ethanol, and finally dried in a vacuum at 60 °C for 6 h. To manipulate the morphologies of the CMSs, 1% $HAuCl_4{\cdot}4H_2O$ with different volumes, such as 1.00, 3.00, and 5.00 mL, were injected into the Cu_2O colloid solutions under the same condition, respectively.

The bare Au NPs were obtained by removing portions of Cu_2O in Cu_2O-Au CMSs under acidic conditions.

2.3. Characterization

X-ray powder diffraction (XRD) analysis was characterized using a Rigaku D/MAX 3C X-ray diffractometer with Cu Kα radiation (λ = 1.5418 Å). X-ray photoelectron spectra (XPS) analysis was conducted using a Thermo Scientific ESACLAB 250Xi A1440 system. UV–vis-NIR absorption spectra were studied using a Shimadzu 3600 spectrometer. Scanning electron microscopic (SEM) images and energy dispersive spectroscopy (EDS)-mappings were obtained using a JEOL 7800 F scanning electron microscope operated at an accelerating voltage of 5.0 kV. Transmission electron microscopic (TEM) images were performed using a Hitachi H-800 transmission electron microscope operated at an accelerating voltage of 200 kV.

2.4. SERS measurement

For SERS experiments, 4-MBA was used as the probe molecule. 4-MBA solution was prepared with the absolute ethanol, and the concentration was 10^{-3} M. The Cu_2O-Au CMSs substrate was incubated in the 4-MBA solution for 4 h. After the precipitate was centrifuged and dried, the SERS spectrum of the sample drop-casted onto the glass slide was recorded in a Horiba–Jobin-Yvon LabRAM ARAMIS spectrometer equipped with a 633 nm He-Ne exciting laser with an effective power of 0.75 mW reaching the sample. The laser was focused on the surface of the sample through a 50 × long-distance objective lens with a 1 μm spot size. SERS spectra were obtained with the acquisition time of 30 s and collecting number of twice using a holographic grating of 1200 grooves/mm. The Raman band of the silicon wafer at 520.7 cm^{-1} was employed to calibrate the spectrometer.

3. Results and discussion

3.1. Preparation and characterization of Cu_2O-Au CMSs

In the preparation of the octahedral Cu_2O microcrystals, the prepared dark blue solution was copper citrate, well known as Benedict's solution, which can be reduced by reducing saccharides, such as glucose, thus reducing Cu^{2+} to Cu^{+} to form the Cu_2O crystals. Meanwhile, in the proposed reaction system, we added the modifier PVP, which was acted as both a stabilizer and a shape-controller to assist in the formation of the Cu_2O octahedrons [30].

After $HAuCl_4{\cdot}4H_2O$ was added into the Cu_2O colloid solution, $AuCl_4^-$ was reduced by Cu_2O. The driving force for the *in situ* reduction of $AuCl_4^-$ to Au NPs on the surface of the Cu_2O microcrystals is attributed to the normal electrode potential difference between $AuCl_4^-$/Au (0.99 V versus normal hydrogen electrode (NHE)) and Cu^{2+}/Cu_2O (0.203 V versus NHE) [31]. The reduced production (Au NPs) was homogeneously deposited on the surface of the Cu_2O microcrystals to lower the surface energy in the system. With the increase in the added volume of the $HAuCl_4{\cdot}4H_2O$ solution, the density of the Au NPs on the surface of the Cu_2O microcrystals was enhanced firstly in the production of Cu_2O-Au CMSs, after which the perfect Cu_2O-Au core-shell heterostructure was obtained, as shown in Scheme 1.

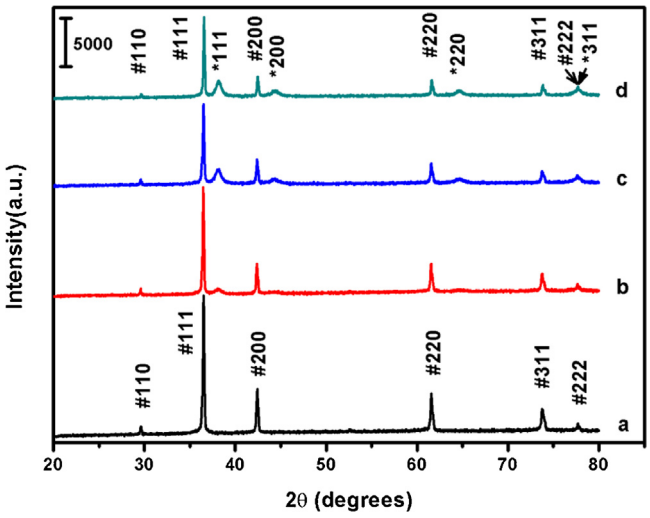

Fig. 1. XRD patterns of the octahedral Cu_2O microcrystals after injecting different volumes of the $HAuCl_4{\cdot}4H_2O$ solutions: (a) 0.00, (b) 1.00, (c) 3.00, and (d) 5.00 mL. The diffraction peaks of Cu_2O are labeled with #, and the diffraction peaks of Au are marked with *.

Once the materials were synthesized, they were characterized by a variety of techniques. Firstly, they were analyzed using XRD. The XRD patterns of the as-prepared octahedral Cu_2O microcrystals displayed diffraction peaks at 2θ = 29.6, 36.5, 42.4, 61.6, 73.8, and 77.7°, corresponding to the {110}, {111}, {200}, {220}, {311}, and {222} lattices in Cu_2O (JCPDS: 05-0667) [29], respectively (Fig. 1a). As is shown in Fig. 1, the diffraction peaks of Cu_2O become weaker, and the new emerging diffraction peaks become stronger with increases in the added volume of the $HAuCl_4{\cdot}4H_2O$ solution. The new diffraction peaks are attributed to the production of Au NPs, located at 38.2, 44.4, 64.6, and 77.7°, which can be indexed to the {111}, {200}, {220}, and {311} planes of crystalline Au (JCPDS: 65-2870) [32], respectively (Fig. 1b–d). These results indicate that Au NPs were coated on the surface of the octahedral Cu_2O microcrystals, but Cu_2O was still the most dominant component in the composites.

Further characterization of the materials was done by employing SEM, EDS-mapping, and TEM analysis. The well-defined octahedral Cu_2O microcrystals with a diameter of about 1.4 μm (Fig. 2e) were synthesized according to the above procedure, and the surface was smooth (Figs. 2 a, e, i, and S2). With the addition of the $HAuCl_4{\cdot}4H_2O$ solution, quasi-spherical Au NPs with a size of 10–50 nm were coated on the surface of Cu_2O (Fig. 3d–f). When the added volume of the $HAuCl_4{\cdot}4H_2O$ solution was 1.00 mL, the diameter of the Cu_2O-Au CMSs was about 1.3 μm (Fig. 2f); Au NPs were uniformly coated on the surface of Cu_2O, and there was some Cu_2O surface exposed (Fig. 3d). In addition, we can clearly identify the nanoholes on the surface of Cu_2O (Fig. 2j), which can further prove that Cu_2O was reduced by $AuCl_4^-$ during the preparation process. With the increase in the volume of the $HAuCl_4{\cdot}4H_2O$ solution to 3.00 mL, due to further Cu_2O etching, the diameter of the Cu_2O-Au CMSs decreased to 1.2 μm (Fig. 2g). The interparticle spacing between the Au NPs became close (Fig. 3e). Further increase in the volume of the $HAuCl_4{\cdot}4H_2O$ solution to 5.00 mL resulted in perfect Cu_2O-Au core-shell heterostructures; a thick Au NPs shell (about 156 nm) was wrapped around the octahedral Cu_2O core (Fig. 3f) and the diameter of the Cu_2O-Au core-shell heterostructure increased

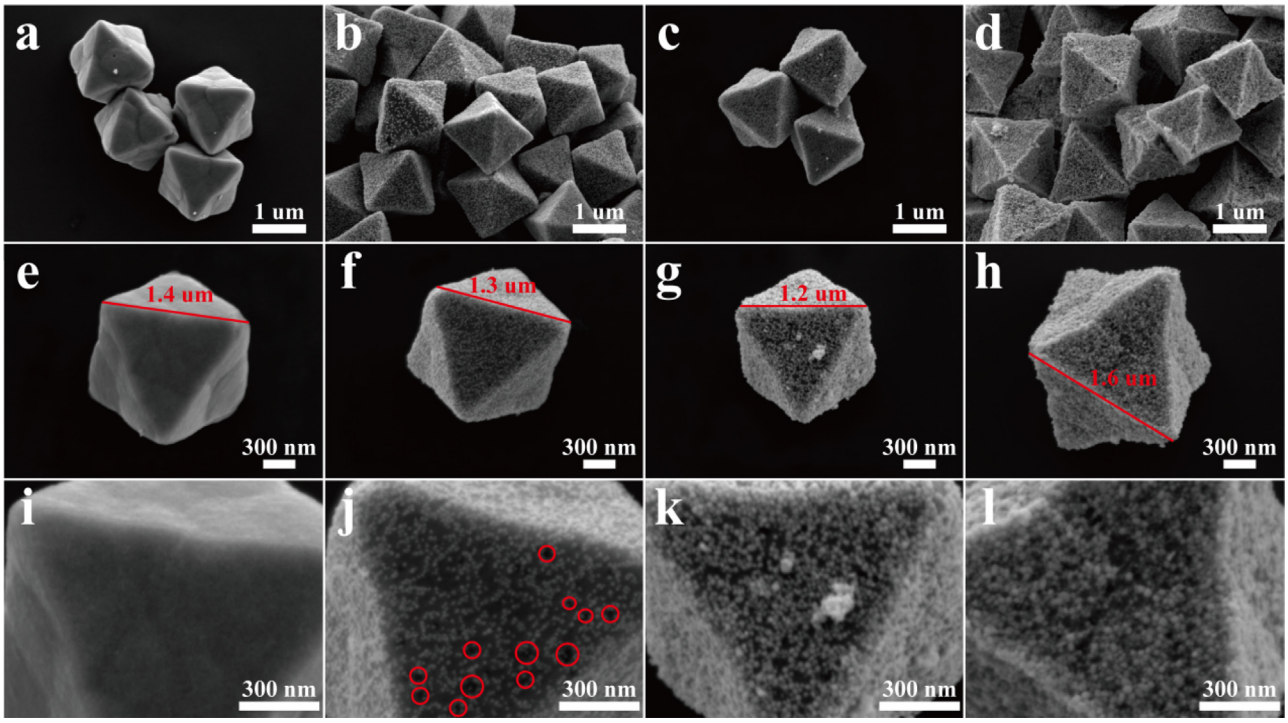

Fig. 2. SEM images with different magnifications of (a, e, i) the octahedral Cu2O microcrystals, and Cu2O-Au CMSs with the addition of different amounts of the gold precursor: (b, f, j) 1.00, (c, g, k) 3.00, and (d, h, l) 5.00 mL. The nanoholes induced by Cu2O etching were marked with circles (j). The diameters of the octahedral Cu2O microcrystals and Cu2O-Au CMSs were about 1.4, 1.3, 1.2, and 1.6 μm, respectively, marked with lines (e-h).

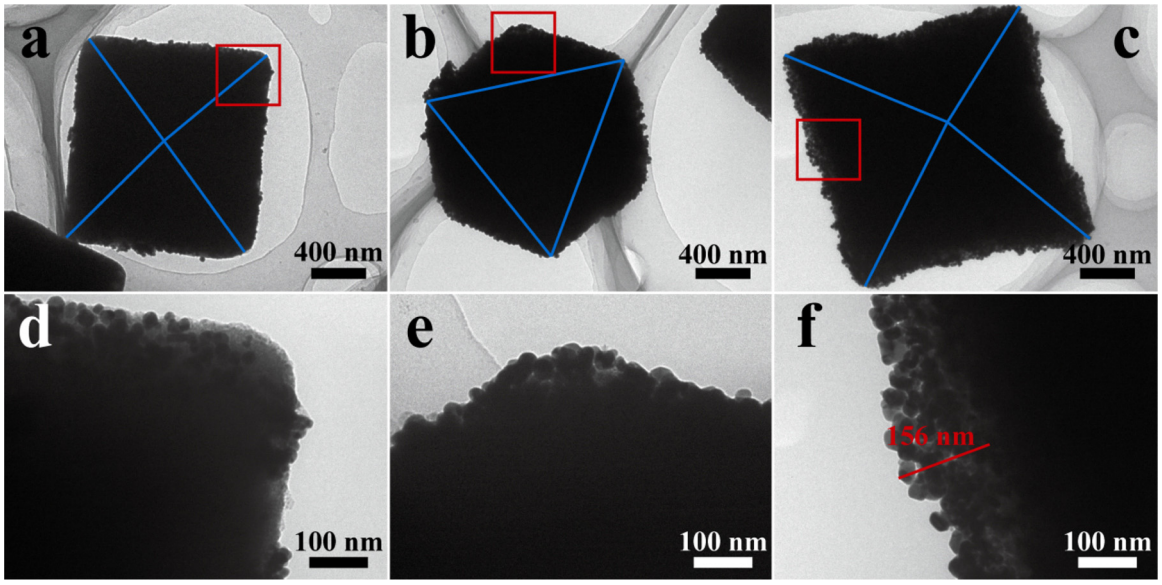

Fig. 3. TEM images with different magnifications of Cu_2O-Au CMSs with the addition of different volumes of the $HAuCl_4{\cdot}4H_2O$ solutions: (a, d) 1.00, (b, e) 3.00, and (c, f) 5.00 mL.

to 1.6 μm (Fig. 2h). The EDS-mapping analysis clearly shows that the Au NPs homogeneously covered the surface of the octahedral Cu_2O microcrystal (Fig. 4).

The UV–vis-NIR spectra of the octahedral Cu_2O microcrystals and Cu_2O-Au CMSs with different amounts of Au NPs are shown in Fig. 5. The spectrum of the octahedral Cu_2O microcrystals shows absorption bands at 532, 639, and 920 nm, which are all strong (Fig. 5a). According to the band energy of Cu_2O [33,34], the absorption band at 532 nm is attributed to the interband transitions in Cu_2O. We presume that the NIR absorbance at 920 nm arises from the excitations of the free carriers in Cu_2O, potentially with plasmonic contributions [33,35]. We can observe the formation of the Au aggregates on the surface of Cu_2O (Fig. 3d–f), but due to the strong absorption peaks of the Cu_2O microcrystals, the plasmon resonance peak of the Au aggregates coupled with the absorption peaks of Cu_2O (Fig. 5b–d). A distinct plasmon resonance peak for the Au aggregates is not observed (Fig. 5b–d). Compared with octahedral Cu_2O microcrystals, the spectra of Cu_2O-Au CMSs with an increasing number of Au NPs are firstly shown blue-shifted (Fig. 5b, c), and finally resolved in the red shift (Fig. 5d). The octahedral Cu_2O microcrystals and Cu_2O-Au CMSs exhibited color changing from brick red to black with increasing amounts of Au NPs (Fig. S1, SI),

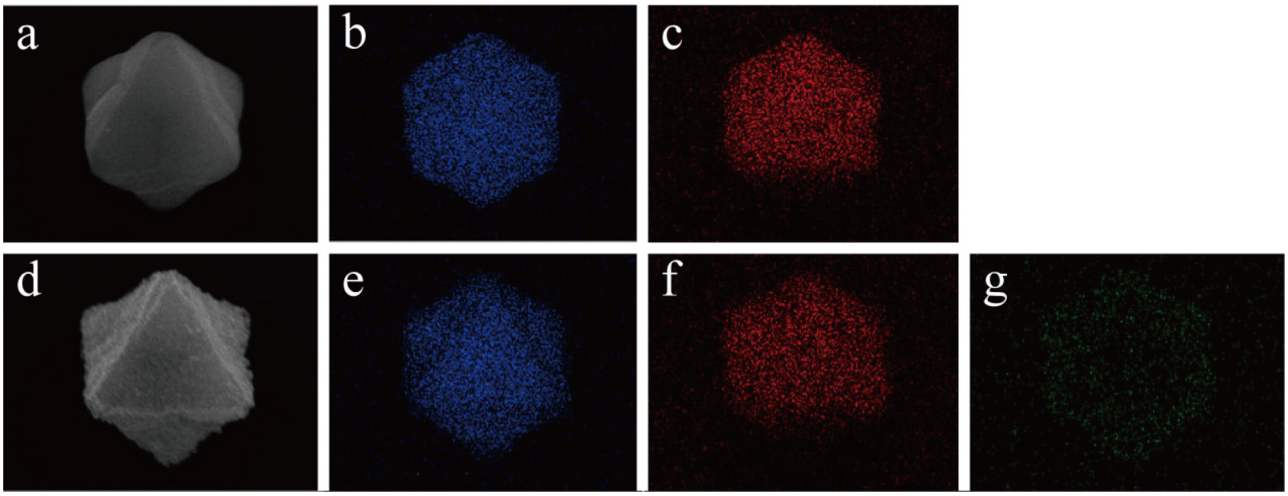

Fig. 4. EDS mappings of (a–c) the octahedral Cu_2O microcrystal and Cu_2O-Au CMS (5.00 mL $HAuCl_4{\cdot}4H_2O$ solution used) (d–g). (a, d) SEM images, (b, e) Cu maps, (c, f) O maps of the Cu_2O microcrystal and Cu_2O-Au CMS, respectively, and (g) Au map of Cu_2O-Au CMS.

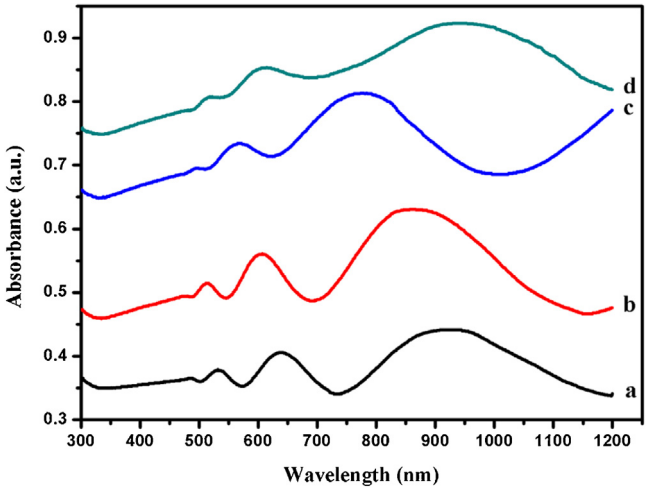

Fig. 5. UV–vis-NIR spectra of (a) the octahedral Cu_2O microcrystals, and Cu_2O-Au CMSs with the addition of different amounts of gold precursor: (b) 1.00, (c) 3.00, and (d) 5.00 mL.

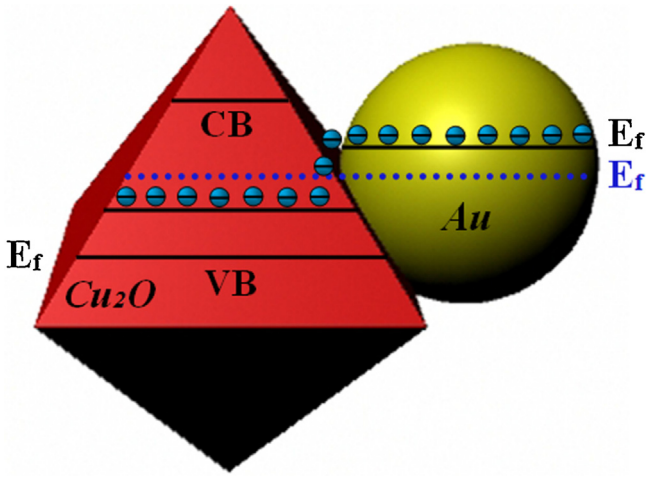

Scheme 2. Fermi level equilibration in a Cu_2O-Au CMSs system.

and this dramatic change can be related to the Cu_2O-Au interaction. As illustrated in Scheme 2, the Fermi level values of Au and Cu_2O are +0.45 V versus NHE and +0.47 V versus NHE, respectively [36,37]. Electrons could transfer from Au to Cu_2O, resulting in a positively charged Au and a negatively charged Cu_2O, and a strong interaction is produced between the Au NPs and Cu_2O microcrystals. Furthermore, this was evidenced by the XPS analysis (Fig. S3, SI), wherein the surface plasmon absorption of Au shifted slightly towards an upward binding energy than that of the bulk Au^0, which was reported to be 84.0 eV [38–40] and was attributed to the charge transfer from Au to Cu_2O. When lower amounts of the Au NPs coated on the surface of the octahedral Cu_2O microcrystals, the absorption peaks of Cu_2O-Au CMSs blue-shifted, which may be primarily caused by the electronegativity increase of the Cu_2O surface induced by the charge redistribution (Fig. 5b, c). Further increasing the volume of the $HAuCl_4{\cdot}4H_2O$ solution, the Au NPs shell wrapped around the octahedral Cu_2O core was produced (Fig. 3f), and the plasmon resonance of the Au aggregates strengthened. Then, the whole structure (Cu_2O-Au CMSs) red-shifted to the near-infrared region (Fig. 5d).

3.2. SERS study of Cu_2O-Au CMSs

Fig. 6 shows the Raman spectra of the octahedral Cu_2O microcrystals and 4-MBA (10^{-3} M) adsorbed on the octahedral Cu_2O microcrystals. It is found that the two spectra are similar. Both spectra show that four bands are associated with Cu_2O at around 214, 420, 509, and 597 cm^{-1} [29,41], and no Raman bands for 4-MBA are observed, which indicates the absence of the SERS effect on the octahedral Cu_2O microcrystals. Subsequently, the SERS spectra of 4-MBA (10^{-3} M) adsorbed on Cu_2O-Au CMSs with different amounts of Au NPs are compared in Fig. 7A. The distinct 4-MBA SERS signals are observed on Cu_2O-Au CMSs [Fig. 7A (a–c)]; the bands are around 846, 1013, 1075, 1143, 1180, and 1584 cm^{-1} [42,43]. The SERS peak intensity of Cu_2O-Au CMSs initially increased [Fig. 7A (a, b)], and then decreased [Fig. 7A (c)]. Furthermore, the SERS peak intensity of Cu_2O-Au CMSs [3.00 mL $HAuCl_4{\cdot}4H_2O$ solution used, Fig. 7A (b)] is also stronger than that of the bare Au NPs [Fig. 7A (d)].

In the Cu_2O-Au CMSs system, the charge transferred from the Au NPs to the Cu_2O microcrystals until the two systems attained equilibration; the redistribution resulted in a positively charged Au and a negatively charged Cu_2O (Scheme 2). When the visible light is incident on the metal surface, the free electron condition leads to a dielectric constant of the metal composed of a large negative real component and a small imaginary component. For the SERS intensity, it is the electromagnetic field at or near the particle

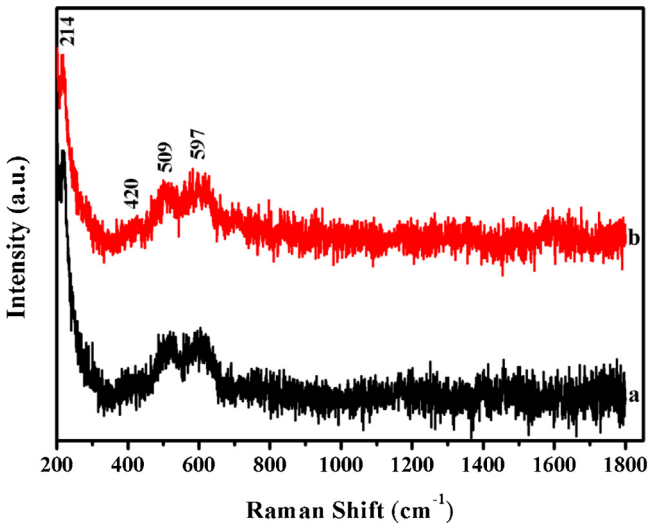

Fig. 6. Raman spectra of (a) the octahedral Cu_2O microcrystals, and (b) 4-MBA (10^{-3} M) adsorbed on the octahedral Cu_2O microcrystals.

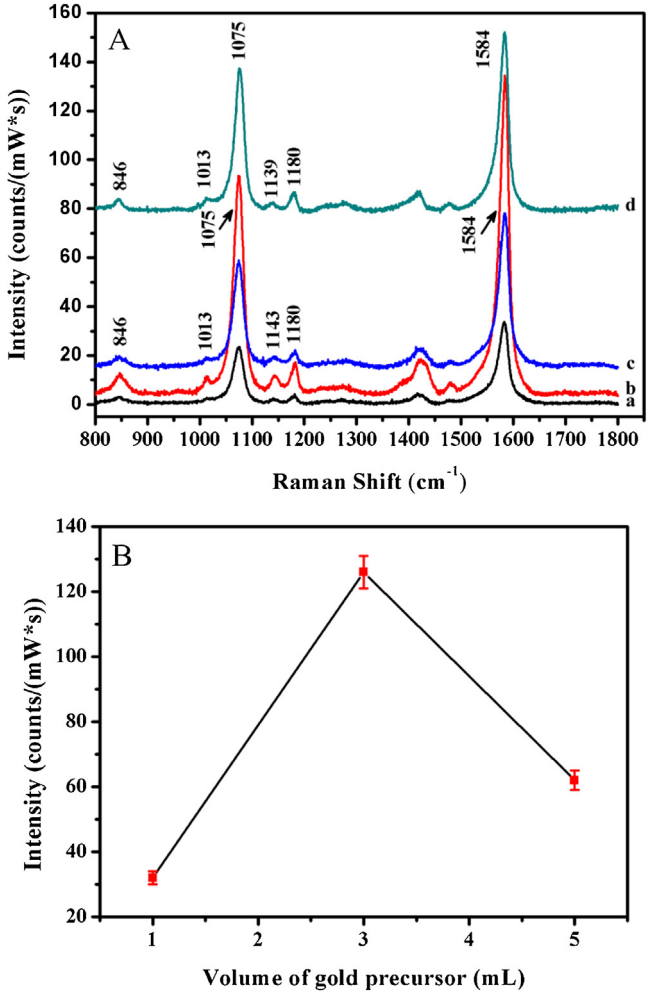

Fig. 7. (A) SERS spectra of 4-MBA (10^{-3} M) adsorbed on Cu_2O-Au CMSs with the different added volumes of the gold precursor: (a) 1.00, (b) 3.00, and (c) 5.00 mL, and (d) the bare Au NPs. (B) SERS intensities with increasing volumes of the gold precursor. Error bars indicate the standard deviations from five independent measurements.

surface that determines the measured intensity. Thus, if $E(\omega)$ is the local field for frequency ω, then the SERS intensity is determined by $<E(\omega)|^2|E(\omega\acute{\imath})|^2>$, where $\omega\acute{\imath}$ is the Stokes-shifted frequency and brackets are used to denote an average over the particle surface. When the Cu_2O microcrystals were coupled with the Au NPs, the interaction between Cu_2O and Au was determined by the polarization induced in each particle due to the fields (E) arising from the charge separation [19]. Compared with the bare Au NPs, the Au NPs coated on the surface of the octahedral Cu_2O microcrystals would excite a more intense LSPR under the irradiation of a suitable laser due to the charge redistribution. In addition, the SERS peak intensity of Cu_2O-Au CMSs was first increased (from 1.00 to 3.00 mL), and then decreased (from 3.00 to 5.00 mL) (Fig. 7B). We suspect the overloading of Au NPs on the surface of the Cu_2O microcrystals would effectively cover the most interfacial Cu_2O-Au SERS active sites and reduce the enhancement [16].

In the proposed study, the main contributions of SERS are the aggregation of the Au NPs and the charge redistribution between the Au NPs and Cu_2O microcrystals, which induces an intense electromagnetic field. We estimate the SERS EF by using the following relationship:

$$EF = (I_{SERS}/I_{NR})(N_{NR}/N_{SERS}) \quad (1)$$

Where I_{SERS} and I_{NR} are the SERS intensities of 4-MBA on the Cu_2O-Au CMSs and normal Raman scattering intensity of the solid sample of 4-MBA (Fig. S4, SI), respectively. N_{NR} and N_{SERS} are the numbers of the 4-MBA molecule adsorbed on the Cu_2O-Au CMSs and bulk molecule illuminated by the 633 nm laser excitation to obtain the corresponding SERS and normal Raman spectra, respectively. In our experiment, the laser spot is 1 μm in diameter and the penetration depth is 17 μm of the focused laser beam used; the density of 4-MBA is 1.345 g/cm^{-3}, thus the number of the 4-MBA molecule illuminated by the laser light is calculated to be 7.01×10^{10}. N_{SERS} is the number of surface-adsorbed molecules within the laser spot that can be obtained according to the method proposed by Orendorff et al. [43].

$$N_{SERS} = N_d A_{laser} A_N/\sigma \quad (2)$$

Where N_d is the density of the Au NPs, A_{laser} is the area of the focal spot of the laser, A_N is the Au NP's footprint area, and σ is the surface area occupied by an adsorbed molecule. Generally, N_d and A_N are obtained from SEM images. A_{laser} can be obtained from the diameter of the laser spot (1 μm) and σ can be adopted as 0.20 nm^2/molecule [44]. Full coverage limit of the 4-MBA molecules on the Cu_2O-Au CMSs surface results in the EF at the Cu_2O-Au CMSs substrate for the band located at 1584 cm^{-1} to have a minimum value of 7.2×10^5.

4. Conclusions

In summary, we have designed a Cu_2O-Au CMSs system that induced CT from Au NPs to Cu_2O microcrystals for the SERS study. This system employed $AuCl_4^-$ as the precursor, which can be reduced by Cu_2O at the room temperature according to the difference in normal electrode potential between $AuCl_4^-$/Au and Cu^{2+}/Cu_2O. The production of Au NPs deposited on the surface of the octahedral Cu_2O microcrystals reduced the surface energy in the system. The density of the Au NPs on the surface of the octahedral Cu_2O microcrystals can be controlled by tuning the concentration of the gold precursor, which can further influence the SERS activity of the Cu_2O-Au CMSs system. In addition, 4-MBA was employed as the probe molecule to evaluate the SERS enhancement from the proposed Cu_2O-Au CMSs heterostructures, which helped us understand the enhancement of the proposed system. The SERS properties of 4-MBA adsorbed on Cu_2O-Au CMSs with different amounts of Au NPs were investigated. Due to the charge transfer

from the Au NPs to the Cu_2O microcrystals, a stronger enhanced electromagnetic field was produced between the interface of the metal and the semiconductor.

Acknowledgements

This work was supported by the National Natural Science Foundation [grant number 61575080 and 21546013] of PR China; the Development Program of the Science and Technology of Jilin Province [grant numbers 20120359, 20140519003JH, 20150520015JH, 20150519024JH, and 20160101287JC]; the Project of Jilin Provincial Environmental Protection Department [grant number 2014-12]; the Scientific Foundation for Young Scientists of Jilin Normal University [grant number 2014004].

Appendix A. Supplementary data

Supplementary data associated with this article can be found, in the online version, at http://dx.doi.org/10.1016/j.colsurfa.2016.07.053.

References

[1] A. Michota, J. Bukowska, J. Raman Spectrosc. 34 (2003) 21.
[2] Z.Q. Tian, B. Ren, Annu. Rev. Phys. Chem. 55 (2004) 197.
[3] K. Kneipp, M. Moskovits, H. Kneipp, Surface-Enhanced Raman Scattering-Physics and Applications, Springer, Berlin, Heidelberg, 2006.
[4] E.C. Le Ru, P.G. Etchegoin, M. Meyer, J. Chem. Phys. 125 (2006) 204701.
[5] W.E. Smith, Chem. Soc. Rev. 37 (2008) 955.
[6] D. Graham, R. Goodacre, Chem. Soc. Rev. 37 (2008) 883.
[7] M. Moskovits, Rev. Mod. Phys. 57 (1985) 783.
[8] H. Metiu, Prog. Surf. Sci. 17 (1984) 153.
[9] J.R. Lombardi, R.L. Birke, J. Phys. Chem. C 112 (2008) 5605.
[10] Z.Q. Tian, B. Ren, D.Y. Wu, J. Phys. Chem. B 106 (2002) 9463.
[11] A.V. Whitney, B.D. Myers, R.P. Van Duyne, Nano Lett. 4 (2004) 1507.
[12] W. Li, Pedro H.C. Camargo, X. Lu, Y. Xia, Nano Lett. 9 (2009) 485.
[13] L. Yang, X. Jiang, W. Ruan, B. Zhao, W. Xu, J.R. Lombardi, J. Phys. Chem. C 112 (2008) 20095.
[14] L. Yang, M. Gong, X. Jiang, D. Yin, X. Qin, B. Zhao, W. Ruan, J. Raman Spectrosc. 46 (2015) 287.
[15] Y. Wang, Z. Sun, H. Hu, S. Jing, B. Zhao, W. Xu, C. Zhao, J.R. Lombardi, J. Raman Spectrosc. 38 (2007) 34.
[16] S. Hsieh, P.Y. Lin, L.Y. Chu, J. Phys. Chem. C 118 (2014) 12500.
[17] D.H. Yu, X. Yu, C. Wang, X.C. Liu, Y. Xing, ACS Appl. Mater. Interfaces 4 (2012) 2781.
[18] X. He, C. Yue, Y. Zang, J. Yin, S. Sun, J. Li, J. Kang, J. Mater. Chem. A 1 (2013) 15010.
[19] G. Shan, L. Xu, G. Wang, Y. Liu, J. Phys. Chem. C 111 (2007) 3290.
[20] X.W. Liu, Langmuir 27 (2011) 9100.
[22] J. Zhang, J. Liu, Q. Peng, X. Wang, Y. Li, Chem. Mater. 18 (2006) 867.
[23] P. Rai, R. Khan, S. Raj, S.M. Majhi, K.K. Park, Y.T. Yu, I.H. Lee, P.K. Sekhar, Nanoscale 6 (2014) 581.
[24] T. Minami, H. Tanaka, T. Shimakawa, T. Miyata, H. Sato, Jpn. J. Appl. Phys. 43 (2004) L917.
[25] D. Cao, C. Wang, F. Zheng, W. Dong, L. Fang, M. Shen, Nano Lett. 12 (2012) 2803.
[26] A. Kudelski, W. Grochala, M. Janik-Czachor, J. Bukowska, A. Szummer, M. Dolata, J. Raman Spectrosc. 29 (1998) 431.
[27] C. Qiu, Y. Bao, N.L. Netzer, C. Jiang, J. Mater. Chem. A 1 (2013) 8790.
[28] L. Yang, J. Lv, Y. Sui, W. Fu, X. Zhou, J. Ma, Q. Li, M. Sun, Y. Mu, Y. Chen, J. Wang, H. Yang, RSC Adv. 4 (2014) 17249.
[29] L. Yang, J. Lv, Y. Sui, W. Fu, X. Zhou, J. Ma, S. Su, W. Zhang, P. Lv, D. Wu, Y. Mu, H. Yang, CrystEngComm 16 (2014) 2298.
[30] Y. Sui, W. Fu, H. Yang, Y. Zeng, Y. Zhang, Q. Zhao, Y. Li, X. Zhou, Y. Leng, M. Li, G. Zou, Cryst. Growth Des. 10 (2010) 99.
[31] G. Millazzo, S. Caroli, Tables of Standard Electrode Potentials, John Wiley & Sons, New York, 1978.
[32] H. Zhu, M.L. Du, D.L. Yu, Y. Wang, L.N. Wang, M.L. Zou, M. Zhang, Y.Q. Fu, J. Mater. Chem. A 1 (2013) 919.
[33] J.P. Hu, D.J. Payne, R.G. Egdell, P.A. Glans, T. Learmonth, K.E. Smith, J. Guo, N.M. Harrison, Phys. Rev. B 77 (2008) 155115.
[34] S. Nikitine, J.B. Grun, M. Sieskind, J. Phys. Chem. Solids 17 (1961) 292.
[35] E.C. Argibay, X.Q. Bao, C.R. Abreu, M.F. Cerqueira, D.Y. Petrovykh, L. Liu, Y.V. Kolen'ko, J. Colloid Interface Sci. 456 (2015) 219.
[36] V. Subramanian, E.E. Wolf, P.V. Kamat, J. Am. Chem. Soc. 126 (2004) 4943.
[37] A. Paracchino, V. Laporte, K. Sivula, M. Grätzel, E. Thimsen, Nat. Mater. 10 (2011) 456.
[38] J. Huang, W.L. Dai, H. Li, K. Fan, J. Catal. 252 (2007) 69.
[39] I.M. Arabatzis, T. Stergiopoulos, D. Andreeva, S. Kitova, S.G. Neophytides, P. Falaras, J. Catal. 220 (2003) 127.
[40] S. Zhu, S. Liang, Q. Gu, L. Xie, J. Wang, Z. Ding, P. Liu, Appl. Catal. B 119 (2012) 146.
[41] H. Zhang, D. Zhang, L. Guo, R. Zhang, P. Yin, R. Wang, J. Nanosci. Nanotechnol. 8 (2008) 6332.
[42] Y. Wang, W. Ji, H. Sui, Y. Kitahama, W. Ruan, Y. Ozaki, B. Zhao, J. Phys. Chem. C 118 (2014) 10191.
[43] C.J. Orendorff, A. Gole, T.K. Sau, C.J. Murphy, Anal. Chem. 77 (2005) 3261.
[44] K. Kim, J.K. Yoon, J. Phys. Chem. B 109 (2005) 20731.